Acta Materialia 219 (2021) 117237

Contents lists available at ScienceDirect

Acta Materialia

journal homepage: www.elsevier.com/locate/actamat

Full Length Article

Evolution of microstructure and crystallographic texture of Ni-Mn-Ga melt-spun ribbons exhibiting 1.15% magnetic field-induced strain

Anna Wójcik[a,*], Robert Chulist[a], Paweł Czaja[a], Maciej Kowalczyk[b], Przemysław Zackiewicz[c], Norbert Schell[d], Wojciech Maziarz[a]

[a] Institute of Metallurgy and Materials Science, Polish Academy of Sciences, 25 Reymonta Street, Kraków 30-059, Poland
[b] The Faculty of Materials Science and Engineering, Warsaw University of Technology, 141 Wołoska Street, Warsaw 02-507, Poland
[c] Lukasiewicz Research Network, Institute of Non-Ferrous Metals, 5 Sowińskiego Street, Gliwice 44-100, Poland
[d] Institute of Materials Physics, Helmholtz-Zentrum Geesthacht, Max-Planck-Strasse 1, Geesthacht D-21502, Germany

ARTICLE INFO

Article history:
Received 2 May 2021
Revised 24 July 2021
Accepted 7 August 2021
Available online 12 August 2021

Keywords:
Ni-Mn-Ga
Ferromagnetic shape memory alloys
EBSD
Synchrotron diffraction
Crystallographic texture

ABSTRACT

The microstructure and texture evolution of 10M Ni-Mn-Ga melt-spun ribbons were thoroughly evaluated by high-energy synchrotron radiation and electron backscatter diffraction. The as-spun ribbons were subjected to annealing treatment in order to tailor microstructure, atomic order degree, and crystallographic texture. The optimum annealing treatment at 1173 K for 72 h produced a homogenous <100> fiber texture and induced grain growth to the size that spans the entire ribbon thickness. This in turn reduced microstructural constraints for twin variant reorientation in the direction perpendicular to the ribbon surface. On the other hand, a homogenous radial microstructure ensured in-plane stress/strain compatibility giving rise to strain accommodation during variant reorientation. Particular attention was also given to the evaluation of atomic order, which to the largest extent controls the characteristic transformation temperatures. It also lowered the twinning stress to a level sufficiently low for martensitic variant reorientation under magnetic field. As a result, 1.15% magnetic field-induced strain without the aid of mechanical training in the self-accommodated state was achieved.

1. Introduction

Ni-Mn-Ga Heusler alloys have attracted considerable attention since the discovery of magnetic field-induced strain (MFIS) by Ullakko et al. [1]. This property can be leveraged to design materials such as actuators, sensors, energy harvesting devices, and bio-medical pumps for drug delivery with multi-responsive functions changing their shape and dimensions under the influence of external magnetic fields [1–10]. Generally, Ni-Mn-Ga alloys undergo a first-order martensitic transformation from high temperature, high symmetry austenite phase to low temperature, low symmetry martensite, during cooling. Upon heating, the inverse martensitic transformation takes place setting out the framework and conditions for the maximum working temperature of MFIS. Till now, large MFIS on the order of 7.1%, 11.2%, and 12% has been found for single crystalline alloys with 10M, 14M, and NM martensite structures, respectively [2–4]. Despite the considerable strain, the most fundamental drawback of Ni-Mn-Ga alloys is that the use of MFIS is practically confined to single crystalline material. Nevertheless, due to the high costs of single crystals fabrication, polycrystalline Ni-Mn-Ga alloys have been also widely investigated [11]. The main limitation of obtaining large MFIS in polycrystalline-alloys are microstructural constraints originating mainly in grain boundaries hampering twin boundary motion [12–14]. Moreover, they give rise to intergranular fracture. To reduce their negative impact and enhance MFIS, coarse-grained and strongly textured materials have been proposed [15–20]. However, very large grains and strong texture components cause strain/stress incompatibility between neighboring grains. The situation is aggravated by limited strain accommodation capacity due to the insufficient number of independent twining systems and slip deactivation. This effectively impedes twin boundary motion and eventually leads to crack formation. Such a deterioration of functional properties is particularly evident when mechanical training is imposed on polycrystalline samples in order to maximize twinning strain and reduce twinning stress. One of the methods to overcome the incompatibility issue is to introduce a certain degree of porosity [21–26]. This approach was successfully applied by Chmielus et al. in polycrystalline Ni-Mn-Ga foams yielding 2–8.7% MFIS [25]. However, up to now, there is no effective way to bypass

* Corresponding author.
E-mail address: a.wojcik@imim.pl (A. Wójcik).

https://doi.org/10.1016/j.actamat.2021.117237

the incompatibility problem in compact polycrystalline Ni-Mn-Ga materials.

Among the several conventional fabrication methods of polycrystals [27–34], melt-spinning process appears as a feasible option since it allows for a strong fiber texture together with limited thickness (∼20–60 μm) [35–41]. Furthermore, melt-spinning is a single-step process, which allows to obtain alloys of good chemical homogeneity and fine microstructure (the size of grains is much smaller compared to arc-melted or induction-melted alloys) in a form of ribbons or flakes. Additionally, the grain size may be tailored by subsequent annealing procedures to reach the length scale comparable with sample thickness. This in turn enables to get rid of constraints on the sample thickness where a strong <100> fiber texture is exposed. In the horizontal direction, on the other hand, melt-spinning produces a homogenous radial microstructure, which may ensure in-plane stress/strain compatibility and hence, improved functional properties [42–45].

So far, many works have concerned the melt-spun Ni-Mn-Ga ribbons including microstructural characterization and functional properties. Some of them describe the structural aspects, important to control and optimize their functional properties [41–43]. In this work, we provide a comprehensive study of the microstructural and crystallographic aspects of $Ni_{50.2}Mn_{28.3}Ga_{21.5}$ as-spun and heat-treated ribbons. The main aim is to produce a strong fiber texture along the sample thickness and a proper microstructure that is able to accommodate the in-plane strain during twin variant reorientation. The 10M structure is chosen since so far it is characterized by the lowest twinning stress, as it provides the most stable and reliable operation over a large temperature range. To attain these goals, the microstructure, crystallographic texture, and degree of order are carefully monitored with the purpose of increasing the twin boundary mobility within particular grains. As a result, 1.15% MFIS without the aid of mechanical training in the self-accommodated state is achieved.

2. Experimental

A bulk alloy with the nominal composition $Ni_{50.2}Mn_{28.3}Ga_{21.5}$ was prepared by induction melting from high purity metals (> 99.9%) in an argon atmosphere. Then, the ingot was inductively melted in quartz tubes and ejected with 0.25 MPa overpressure onto a copper wheel rotating at a linear speed of 25 m s^{-1}. The ribbons were heat-treated under various conditions: (i) 573 K/1 h, (ii) 873 K/1 h, (iii) 1073 K/1 h, (iv) 1173 K/1 h, and (v) 1173 K/72 h followed by air cooling. The crystal structure and global texture of ribbons were examined by high-energy X-ray diffraction measurements at DESY in Germany, Hamburg, using the beamline P07B (87.1 keV, $\lambda = 0.0142342$ nm). For phase analysis, the diffraction patterns were recorded in the so-called continuous mode using 2D Mar345 Image Plate detector. In order to obtain textureless measurements, all samples were rotated by 180° about the ω-axis when X-rayed. This procedure was the same for all samples. Additionally, samples for X-ray diffraction measurements (phase or texture) were prepared in a "sandwich" form consisting of more than 10 pieces of ribbons to ensure good grain/variant statistics. The beam size was 1×1 mm^2. Subsequently, the obtained 2D patterns were integrated using the Fit2D software and presented in a graph of relative intensity vs. 2Theta angle. The atomic order was calculated as the intensity ratio of I_{hkl}/I_{220} using the reflection of the dominating phase i.e. up to 873 K from austenite reflections and then from martensite ones except for $(123)_{10M}$ which is observed only in the martensitic state. Pole figures were computed with the use of the StressTexCalculator and Labotex softwares [46]. Microstructural observations and structural analysis were carried out by FEI Quanta 3D field emission gun scanning electron microscope (SEM) equipped with Trident energy-dispersive X-ray spectrometer (EDX) produced by EDAX and TSL electron backscattered diffraction (EBSD) system.. Samples for SEM observations were mechanically polished and then etched electrolytically at room temperature with a Struers electropolishing LectroPol-5 using an electrolyte of nitric acid (vol. 1/3) and methanol (vol. 2/3). Thermal effects were investigated by differential scanning calorimetry (DSC) using a thermal analyzer Netzsch DSC 214 Polyma with heating/cooling rate of 10 K/min. Magnetic field-induced strains and the characteristic martensitic and magnetic transformation temperatures were examined by Physical Properties Materials System (PPMS) with VSM mode. Measurements were done in field cooling (FC) and field heating (FH) regimes in the temperature range between 2 and 400 K. The data were recorded with a temperature change rate of 1 K/min. The value of the external field was 50 Oe (4000 A/m). The hysteresis loops were recorded at room temperature (300 K). All the experiments mentioned above were performed on samples situated longitudinally to the external magnetic field. Finally, hysteresis loops at 300 K for the transverse magnetic field were recorded.

3. Results and discussion

3.1. Martensitic transformation

Fig. 1 displays DSC curves for as-spun and heat-treated Ni-Mn-Ga ribbons. The large exothermic and endothermic peaks observed between 280 and 320 K recorded during cooling and heating correspond to the forward and reverse martensitic transformation, respectively. Interestingly, for the melt-spun ribbons and ribbons heat-treated at 573 and 873 K peaks are visibly broadened and split, which may relate to microstructural inhomogeneity, comprising of equiaxed grains as well as larger elongated slab-like shaped grains, atomic disorder and/or internal stresses since the chemical composition has been verified as uniform (SEM/EDS). During annealing, diffusion processes occur ensuring more structural and microstructural homogeneity which is evidenced by almost sharp DSC peaks for high temperature annealed samples. The characteristic martensite start ((M_s^{DSC})), austenite start ((A_s^{DSC})), martensite finish (M_f^{DSC}) and austenite finish ((A_f^{DSC})) temperatures were estimated from DSC curves by the tangent method and are annotated near the respective curves in Fig. 1 (M_s, A_s) as well as listed in Table 1. As it is evidenced, both the M_s and A_s temperatures slightly shift toward higher temperatures with the increase of annealing temperature up to 1173 K being good in line with single crystalline material of the same composition, and then after 72 h they are found to inconsiderably decrease.

Subsequently, the values of martensitic transformation temperatures were confirmed by magnetic measurements. The temperature dependence of magnetization was measured under low external magnetic field $H = 50$ Oe. The field cooling (FC) and field heating (FH) curves of as-spun and heat-treated ribbons are presented in Fig. 2. It is found that there are two abrupt changes of magnetization for all ribbons. With cooling from a temperature of 400 K, a large increase of magnetization is attributed to the paramagnetic-ferromagnetic transition of the $L2_1$ austenite. The Curie temperature (Tc), determined by tangent method, increases with the annealing temperature up to 1173 K, while maintaining the steady value independent of the additional annealing time. This effect can be ascribed to magnetic exchange interaction that is strongly influenced by the Mn-Mn distance and directly linked to atomic order. Generally, in the off-stoichiometric Ni-Mn-Ga alloys, excess Mn atoms occupy not only Mn but also Ga sites typically favoring Mn-Mn antiferromagnetic interaction. With the increase of $L2_1$ order degree, more Mn atoms are in Mn sublattice instead of Ga ones amplifying next-nearest neighbor Mn-Mn ferromagnetic exchange interaction. This mechanism affects the magnetization values and leads to shifting of T_C to higher temperatures [47,48]. With fur-

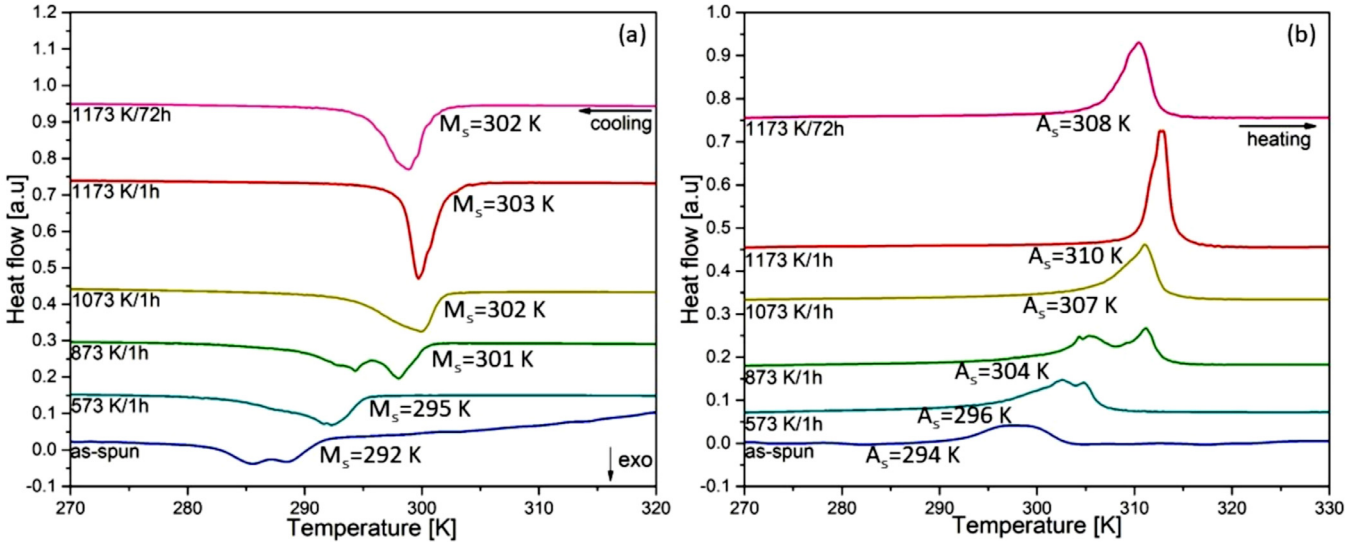

Fig. 1. DSC curves recorded during cooling (a) and heating (b) for as-spun and heat-treated $Ni_{50.2}Mn_{28.3}Ga_{21.5}$ ribbons.

Table 1
Characteristic martensite start ((M_s^{DSC})), austenite start ((A_s^{DSC})), martensite finish (M_f^{DSC}) and austenite finish ((A_f^{DSC})) temperatures, Curie temperature of austenite (T_c), martensite volume fraction and average grain size of $Ni_{50.2}Mn_{28.3}Ga_{21.5}$ ribbons.

Factor	As-spun	573 K/1 h	873 K/1 h	1073 K/1 h	1173 K/1 h	1173 K/72 h
M_s^{mag} (K)	291	292	300	302	305	305
M_s^{DSC} (K)	292	295	301	302	303	302
M_f^{mag} (K)	283	284	297	295	304	304
M_f^{DSC} (K)	282	284	289	294	298	295
A_s^{mag} (K)	290	293	304	306	312	312
A_s^{DSC} (K)	294	296	304	307	310	308
A_f^{mag} (K)	302	305	312	311	317	318
A_f^{DSC} (K)	303	307	312	313	314	313
T_C (K)	363	374	374	375	376	376
Volume fraction of martensite (%)	0	14.1	44.8	70.2	100	100
Grain size (μm)	2.7	3.3	3.5	6.3	9.5	59.4

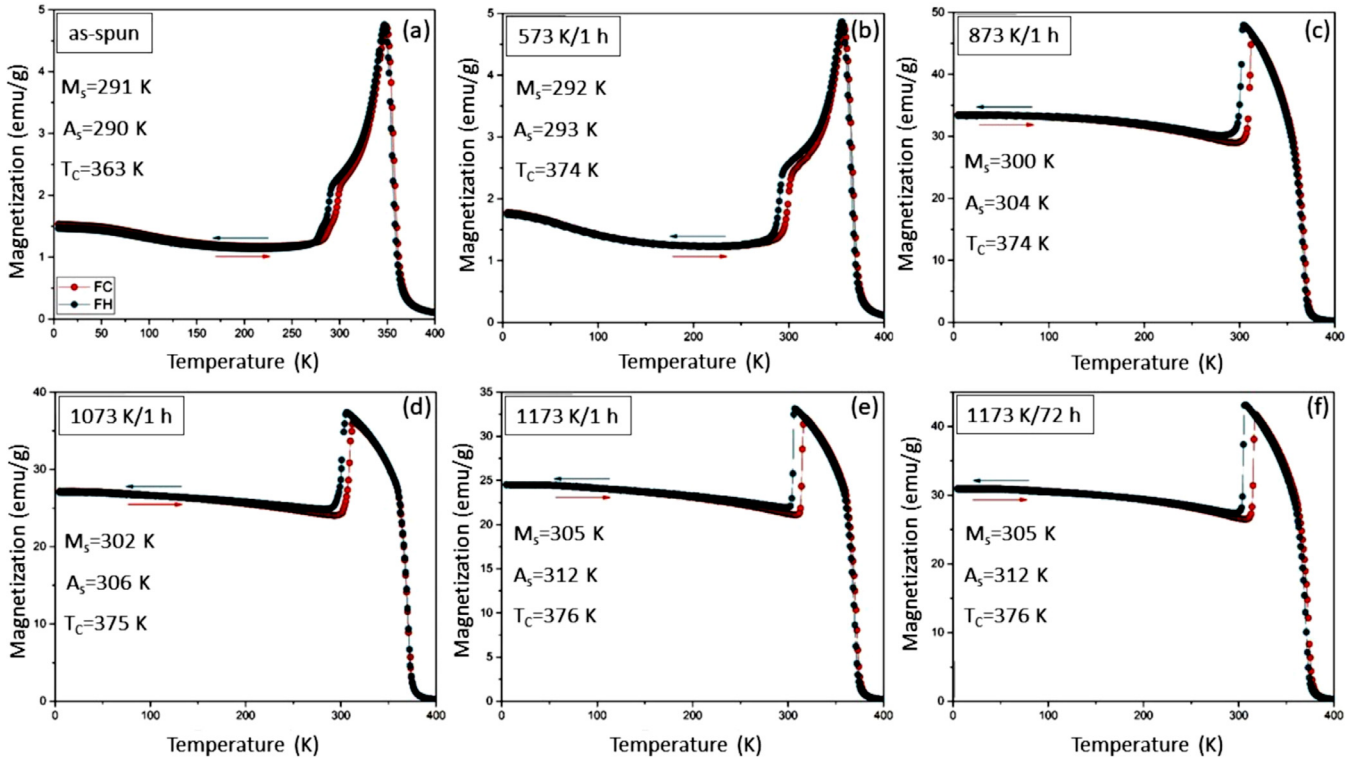

Fig. 2. Magnetization vs temperature curves recorded during field heating (FH) and field cooling (FC) for all ribbons.

ther cooling, a drop of magnetization, due to stronger magnetic anisotropy of the lower symmetry low temperature phase, indicates the martensitic transformation from austenite to martensite. During heating, reverse martensitic transformation takes place. The estimated, by tangent method, the Ms and As temperatures are shown on the charts while all evaluated temperatures are listed in Table 1. The obtained results are in good agreement with DSC ones whereas small discrepancies can be distinguished. It is worth noting that characteristic temperatures for the as-spun and the annealed at 573 K/1 h ribbons determined with magnetic measurements are slightly lower compared to DSC ones, i.e. about 2, 3 degrees, while for the samples treated at higher temperatures an opposite tendency is observed. This appears to be linked to an interaction between magnetic and structural degrees of freedom since in the samples exhibiting disordered structure, the structural rearrangement is revealed first (DSC), while for high-ordered alloys magnetic interaction can be detected earlier (magnetization).

Another issue is the two-stage or "extended" transformation character of DSC curves for as-spun as well as heat-treated at 573 K/1 h and 873 K/1 h ribbons. It can be recognized by the characteristic splitting of DSC peaks observed for all three aforementioned ribbons, whereas M(T) charts confirm this result, by the existence of "humps", only for as-spun and annealed at 573 K/1 h samples (Fig. 2). Interestingly, the effect is not detected in M(T) curve for ribbon annealed at 873 K. It seems that it is due to stabilization of martensitic phase by applying magnetic field. This causes a slight shift of the "second DSC peak" to higher temperature region. Based on both magnetic and DSC curves, the temperature intervals of martensitic transformation for the sample annealed at 873 K/1 h were estimated at 4 K and 13 K, respectively. Generally, the transition range for more ordered samples is narrower for M(T) measurements which implies that even a small magnetic field stabilizes the martensitic phase. This assumption is also confirmed by X-ray diffraction where without the application of magnetic field the samples show a two-phase structure at room temperature. Thus, they are good in line with DSC curves as well as Rietveld analysis where no magnetic field is applied. The effect of the two-stage or extended transformation appears to be linked to inhomogeneous microstructure as discussed in the next paragraph.

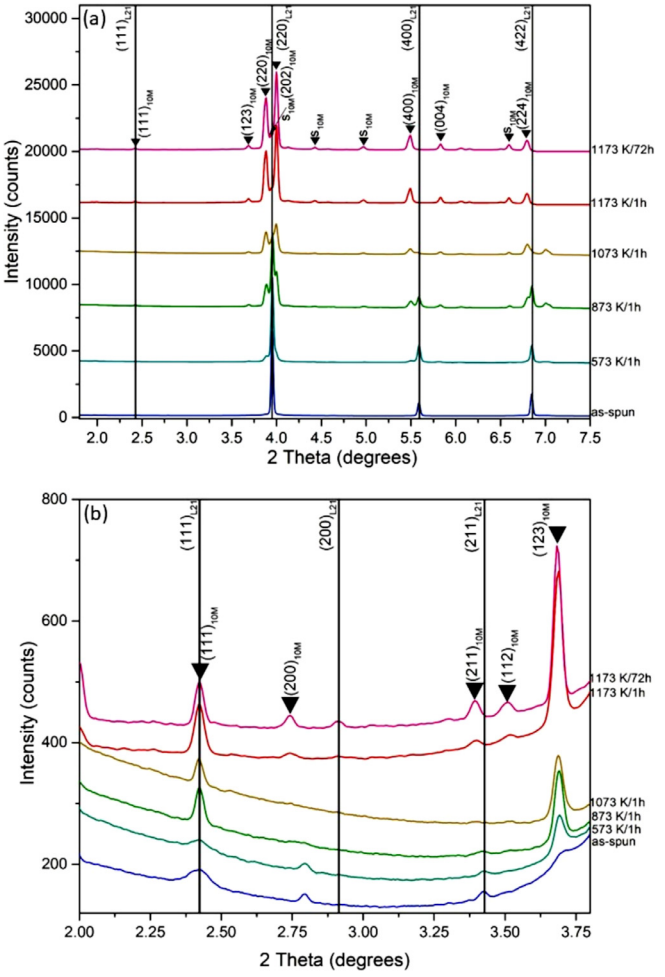

Fig. 3. (a) Room temperature synchrotron X-ray diffraction patterns with a whole range and (b) low-angle area for as-spun and heat-treated $Ni_{50.2}Mn_{28.3}Ga_{21.5}$ ribbons.

3.2. Microstructure and crystallographic texture

Ribbons were also systematically analyzed by means of high energy X-ray diffraction and electron microscopy. Fig. 3(a) presents RT (293 K) synchrotron X-ray diffraction patterns of the as-spun and annealed $Ni_{50.2}Mn_{28.3}Ga_{21.5}$ ribbons. The initial ribbon has a single-phase $L2_1$ austenite microstructure with a small (111) superlattice reflection; see Fig. 3(b) for better visibility. This is well consistent with the initial indication by DSC and VSM, which have detected M_s temperature slightly below 293 K. As it is evidenced with the increase of heat treatment temperature from 573 to 1073 K, the peaks corresponding to martensite appear and the amount of martensite gradually increases, finally attaining 100% volume contribution following annealing at 1173 K for 72 h. The volume fraction of martensite, calculated by the so-called continuum method and Rietveld refinement using the HighScore Plus software, was found to be 14.1, 44.8, 70.2, 97.3, and 100% for ribbons annealed at 573 K/1 h, 873 K/1 h, 1073 K/1 h, 1173 K/1 h, and 1173 K/72 h, respectively, Fig. 4. In the case of heat-treated ribbons, the martensite was assigned according to modulated – five-layered (10M) monoclinic martensite, however, the indexing is given in the so-called parent-based coordinate system i.e., with respect to austenite phase, unless stated otherwise [49,50]. The main goal of such a convention is to bring both phases into coincidence with regard to the sample coordinate system, which then significantly simplifies texture analysis. Therefore, the 10M structure was identified in terms of splitting of the original cubic $(220)_A$ and $(400)_A$ peaks into martensite peaks $(220)_M$, $(022)_M$, $(202)_M$ and $(400)_M$, $(040)_M$, $(004)_M$ as a result of martensitic transformation. For monoclinic long-periodic description of 10M martensite the reader is referred to [51]. No other martensitic structure was confirmed by SEM, TEM or X-ray method which rules out the presence of intermartensitic transformation.

The ternary intermetallic Ni-Mn-Ga compounds may exhibit different types of chemical order. In fact, the chemical composition along with atomic order are two degrees of freedom that can greatly affect the martensitic transformation, magnetic properties, and twinning stress in Ni-Mn-Ga alloys. Generally, the structure factors, F, for the (111) and (200) planes are composed of different terms, hence, they may evolve differently upon heat treatment. On the other hand, F(110) and F(220) are the sum of all four sublattices and should be independent of chemical order [52,53]. To evaluate the states of atomic order of Ni-Mn-Ga ribbons, the intensity ratio of I_{hkl}/I_{220} was calculated. The (220) reflection was chosen as a reference one, because it is orientated far away from the highly textured <100> fiber axis and because it is not supposed to change when samples restore with heat treatment. According to Fig. 5, the $L2_1$ order, represented most distinctly by F(111), gradually increases with annealing temperature up to 1173 K. Extending the annealing time at this temperature has less effect on the F(111). This structure evolution is well in line with the increase of the martensite volume fraction given in Fig. 4 indicating that the

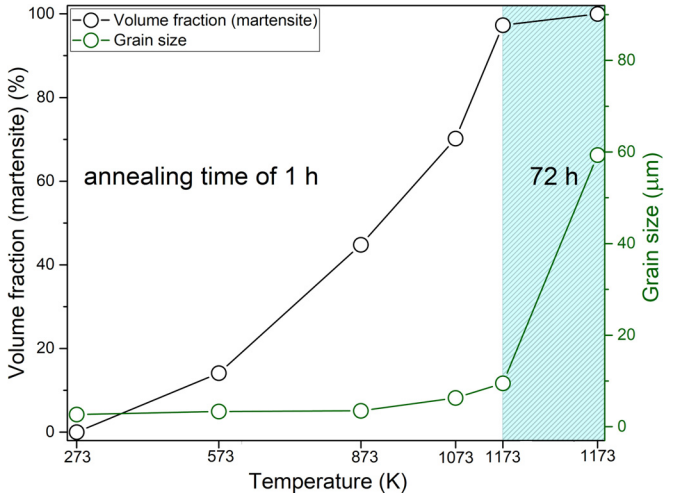

Fig. 4. Dependence of volume fraction of martensite and grain size on annealing conditions of $Ni_{50.2}Mn_{28.3}Ga_{21.5}$ ribbons.

chemical order is the main factor controlling martensitic transformation. The ordering for two other planes, F(200) and F(110) displays a different course of the curve with a sudden fall as the main fraction of material transforms to martensite. This can be attributed to the shear processes along the <110> direction during martensitic transformation, which changes the periodic distortion along with lattice parameters and stacking sequence of the modulated lattice [54]. This is not the case for the (111) plane, which independently of the crystal symmetry yields equal spacing for the whole set of the {111} planes, see Fig. 3b. Fig. 5(b) also shows that for the stoichiometric composition, the $L2_1$ phase can be built up with alternating (111) planes composed of only one type of atom (for instance Mn, Ni or Ga). For these reasons, the F(111) is extremely sensitive to any change in atomic arrangement. Taking into consideration the low angle peaks the evolution of $(123)_{10M}$ peak (expressed in the long periodic coordinate system [51]) as the function of heat treatment temperature was also well observed, Fig. 3(b). Originally, this reflection was not employed to explore the state of atomic order of modulated phase, however as can be seen in Figs. 3 and 5 its progressive increase in intensity can be attributed to a higher degree of order of periodic shuffling. This, in turn, is strictly related to atomic position within the $(123)_{10M}$ plane, Fig. 5(c). In other words, this reflection stands for a proper modulation period and indicates a well-developed 10M structure. For better illustration, the atomic order of $(123)_{10M}$ is shown in Fig. 5b where some positions of unmodulated structure are also depicted (empty circles). In fact, annealing rebuilds the ordered $L2_1$ and then 10M structures which were highly disordered due to a rapid solidification process. This also shows that very fast cooling rates may disorder Ni-Mn-Ga alloys that are considered to be rather ordered with a high tendency to form short-range order.

Fig. 4 summarizes the effect of heat treatment on the grain size (green plot) and the volume fraction of martensite (black plot). As was mentioned above, the martensite volume fraction (at RT) tends to increase with heat treatment temperature and time, reaching 100% for ribbon annealed at 1173 K/72 h. It is related to the shift of martensitic transformation towards higher temperatures, slightly above room temperature, with the annealing temperature. As it was reported, the martensitic transformation behavior, besides chemical composition [55,56] is also sensitive to microstructural features [27,57]. In the presented case, both the effect of grain size and atomic order will be discussed. From Fig. 4 it can be stated that the heat treatment increases the average grain size as the annealing temperature increases up to 1173 K. However, the largest jump of the grain size value, from 9.5 to 59.3 μm, is observed with the extending of heating time from 1 to 72 h. Thus, the largest jump of martensitic transformation should be expected with the increase of annealing time, whereas martensitic transformation temperature states almost constant. This result clearly shows rather a modest impact of the grain size on martensitic transformation temperature. On the other hand, the second considering factor – atomic order appears to affect to a much greater extent the martensitic transformation [47,58]. With the increase of $L2_1$ order degree both MT temperatures increase as well as the martensite volume fraction grows reaching the steady value when the full $L2_1$ ordering is achieved. The effect of atomic order degree includes a related change of electronic structure as well as lattice site occupancy, especially by Mn atoms, and directly impacts both martensitic and magnetic transformations.

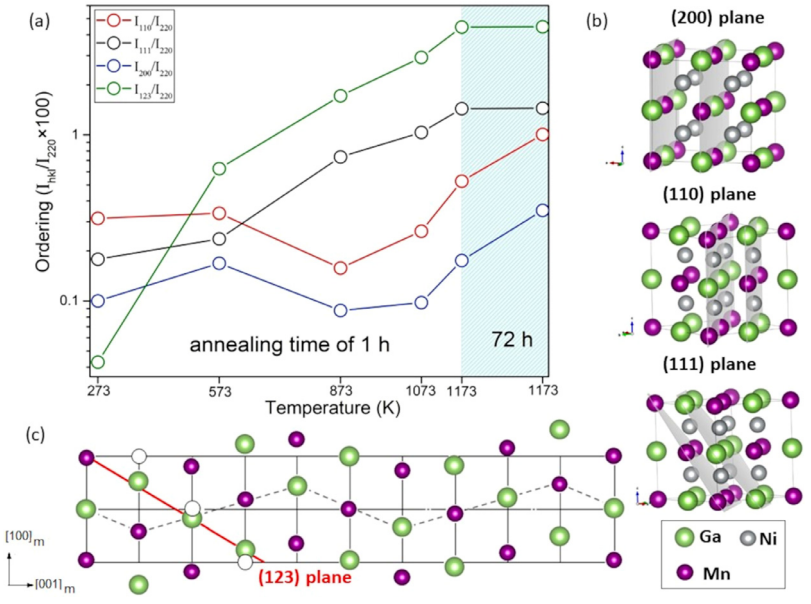

Fig. 5. Relation between ordering degree and heat treatment conditions for $Ni_{50.2}Mn_{28.3}Ga_{21.5}$ ribbons. The (200), (110) and (111) planes are illustrated with respect to parent-based coordinate system (austenite) while the $(123)_{10M}$ plane with regard to long-periodic modulated structure [51].

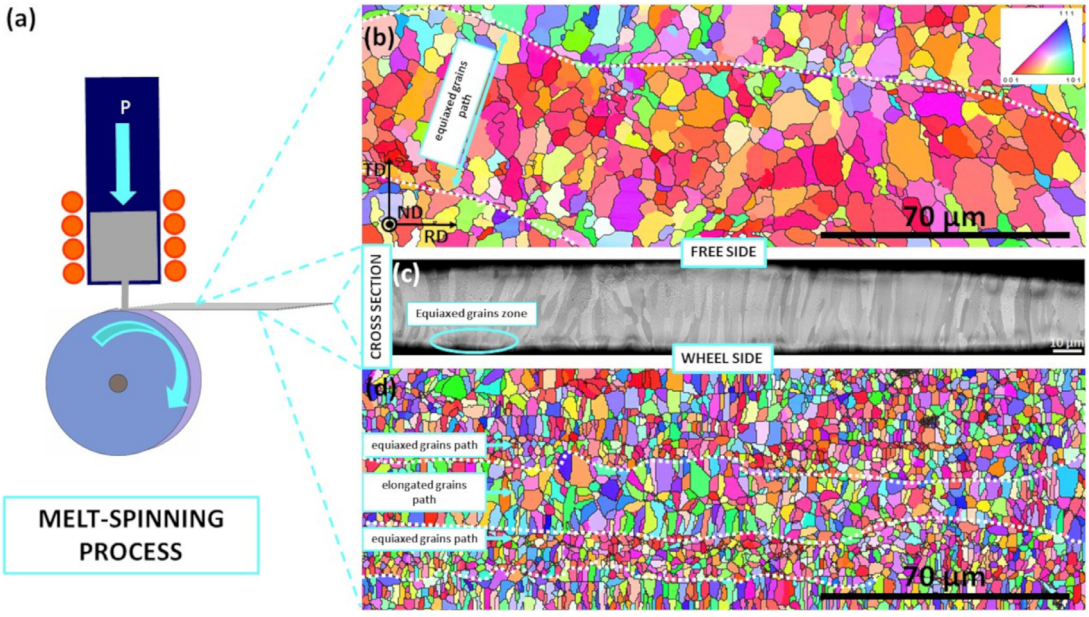

Fig. 6. Scheme of melt-spinning process (a); EBSD map taken from the free side (b) and the wheel side (d); BSE/SEM image of the cross-section for as-spun $Ni_{50.2}Mn_{28.3}Ga_{21.5}$ ribbon.

Fig. 6(a) displays the scheme of melt-spinning process which involves casting of the inductively melted alloy by its ejection with an overpressure onto a rotating copper wheel cooled by water. The molten alloy rapidly solidifies upon contact with the cold surface of the wheel and a thin ribbon is formed. Here, the Ni-Mn-Ga as-spun ribbons were produced in a flake form having 10–20 mm of length, 2–5 mm of width, and around 60 µm of thickness. To clarify the description a wheel side (surface being in the contact with the wheel), a free side and a cross-section were defined. Fig. 6(b) and (d) present exemplary SEM/EBSD orientation maps collected for both the free and the wheel side of the austenitic Ni-Mn-Ga as-spun ribbon. It is shown that both sides differ from each other, mainly, by the grain size and the shape of grains. The average grain size (taken from the large areas) was estimated to be 6.4 ± 3.8 µm and 3.3 ± 1.8 µm for the free and the wheel side, respectively. The difference in size between both sides is a result of various cooling rates during the process. Additionally, the grains at the free side have shapes mainly close to equiaxed while they are arranged in the paths (zones) with the width of 50–70 µm. In the case of the wheel side, the microstructure consists of alternate zones of fine equiaxed grains and larger elongated ones. The paths are arranged with a direction parallel to the roll direction (RD) and were formed during the solidification of thin molten alloy spurts. The SEM/BSE micrograph, Fig. 6(c), displays the cross-section with coarse columnar grains along the ribbon thickness and (smaller of about a few µm) a zone of fine equiaxed grains close to the surface being in a contact with the wheel. It is well known that the growth of columnar grains is strikingly associated with the heat transfer (perpendicular to the ribbon surface) during the solidification process [59].

Fig. 7(a) displays the IPF/EBSD orientation map while Fig. 7(b) shows an image quality (IQ) EBSD map taken from the same large area of the free side of the austenitic Ni-Mn-Ga as-spun ribbon. Here, the crystallization paths can be identified as well as two areas with different grain morphology – (1) small equiaxed grains and (2) elongated into slab-like shape grains. The mean grain size is estimated to be 2.5 ± 0.8 µm and 8.9 ± 3.9 µm in regions 1 and 2, respectively. Moreover, Fig. 7(c) and (d) show the $\{400\}_A$, $\{220\}_A$, $\{111\}_A$ pole figures for austenite for different areas. It is evidenced that region 1 has a strong <100> fiber texture with $\{100\}_A$ parallel to the ribbon plane. This is related to the heat transfer direction during the solidification process (perpendicular to the ribbon surface), and preferential crystallization of austenite grains along the [100] direction resulting in a strong fiber texture with the <100> direction perpendicular to the ribbon plane. The preferred orientation of $\{100\}_A$//ribbon plane has also been described for Ni-Mn-Ga ribbons [42,43,56]. Moreover, taking into account the pole figures measured from region 2, the ribbon also exhibits close to $<100>_A$ fiber-like texture, however, with the grain growth parallel to the transverse direction (TD). This component is also associated with the heat transfer during ribbons casting but in TD due to large length to width aspect. Thus, the as-spun ribbons are characterized with a double <100> fiber texture with the dominating component parallel to ND and minor to TD.

Moreover, the IQ EBSD map shown in Fig. 7 (b) displays brighter and darker areas that correspond to higher or poorer Kikuchi pattern quality. More defected areas are seen as low pattern quality (darker) indicating lower atomic order degree and enhanced defect density. It stands to reason that some areas recover faster than other ones giving rise to two-stage and extended transformation. As was shown before (Fig. 4), the effect of grain size is excluded having basically no impact on phase transformation. This can be also seen in Fig. 8 where much smaller martensitic grains transform earlier than larger austenitic ones.

The EBSD orientation maps for ribbons annealed at 1173 K/1 h and 1173 K/72 h are shown in Fig. 8. A small area of about 150 µm of austenitic grains surrounded by martensitic ones is visible in Fig. 8(a). EBSD maps revealed a twinned microstructure with a larger grain size and a higher amount of twins in ribbons annealed for 72 h. The estimated grain size of both ribbons annealed for 1 h and 72 h was found to be 9.4 ± 3.7 µm and 59.3 ± 28.7 µm, respectively.

Fig. 8 (c) and (d) depict the BSE/SEM images taken along the cross-section of both annealed at 1173 K for 1 h and 72 h ribbons, respectively. The grain size of the annealed ribbons significantly increases with the increase of annealing time. It was estimated that the width of columnar grains raises up to about 9.4 ± 3.7 µm for 1 h and 59.3 ± 28.7 µm for 72 h with respect to as-spun ones with an average width of 2.89 ± 1.1 µm. These results are consistent with plane view SEM observations and also show that the columnar grains span the whole ribbon thickness. This gives rise

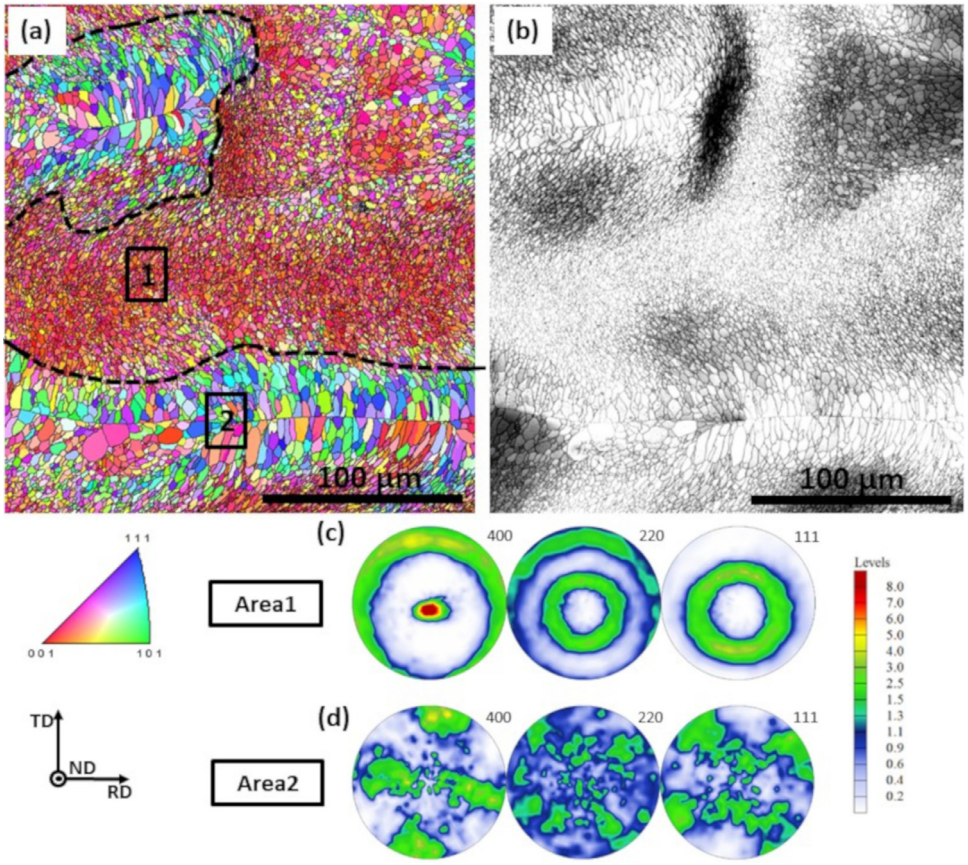

Fig. 7. EBSD map taken from the free side of as-spun $Ni_{50.2}Mn_{28.3}Ga_{21.5}$ ribbon showing two different grain morphology (a), image quality (IQ) EBSD map (b), and corresponding $\{400\}_A$, $\{220\}_A$ and $\{111\}_A$ pole figures (c), (d), where ND $\perp$ ribbon plane.

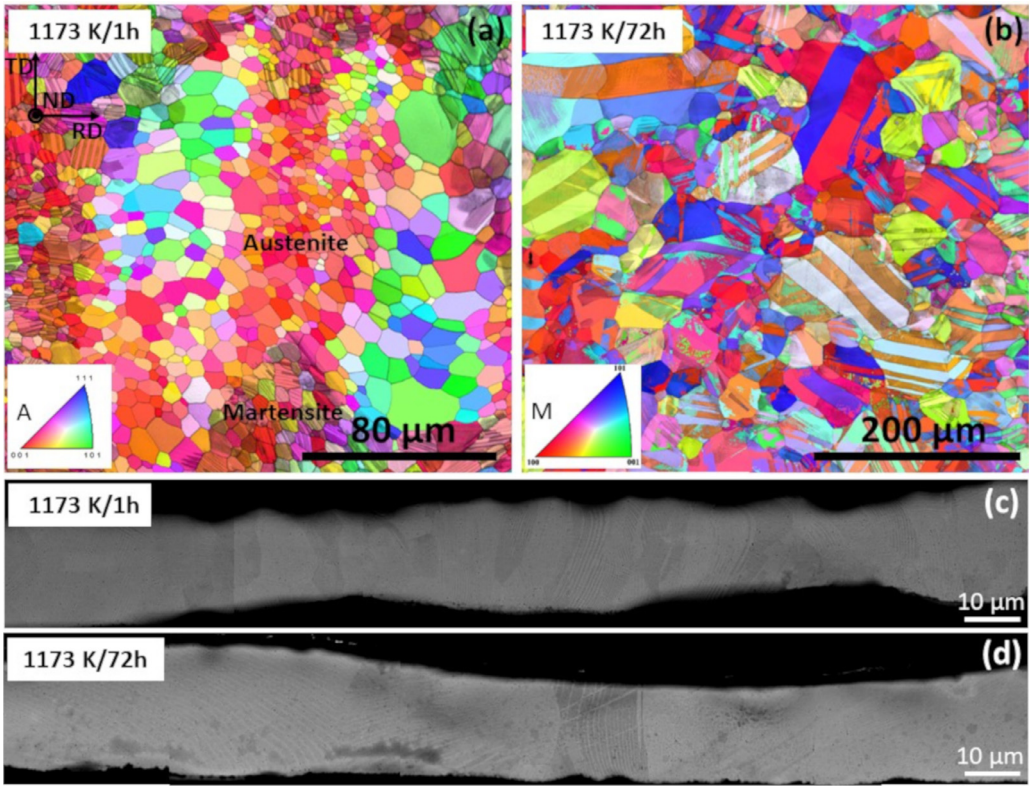

Fig. 8. EBSD maps taken from the free side of Ni-Mn-Ga ribbon annealed at 1173 K/1 h (a) and 1173 K/72 h (b); cross-section of Ni-Mn-Ga annealed at 1173 K/1 h (c) and 1173 K/72 h (d).

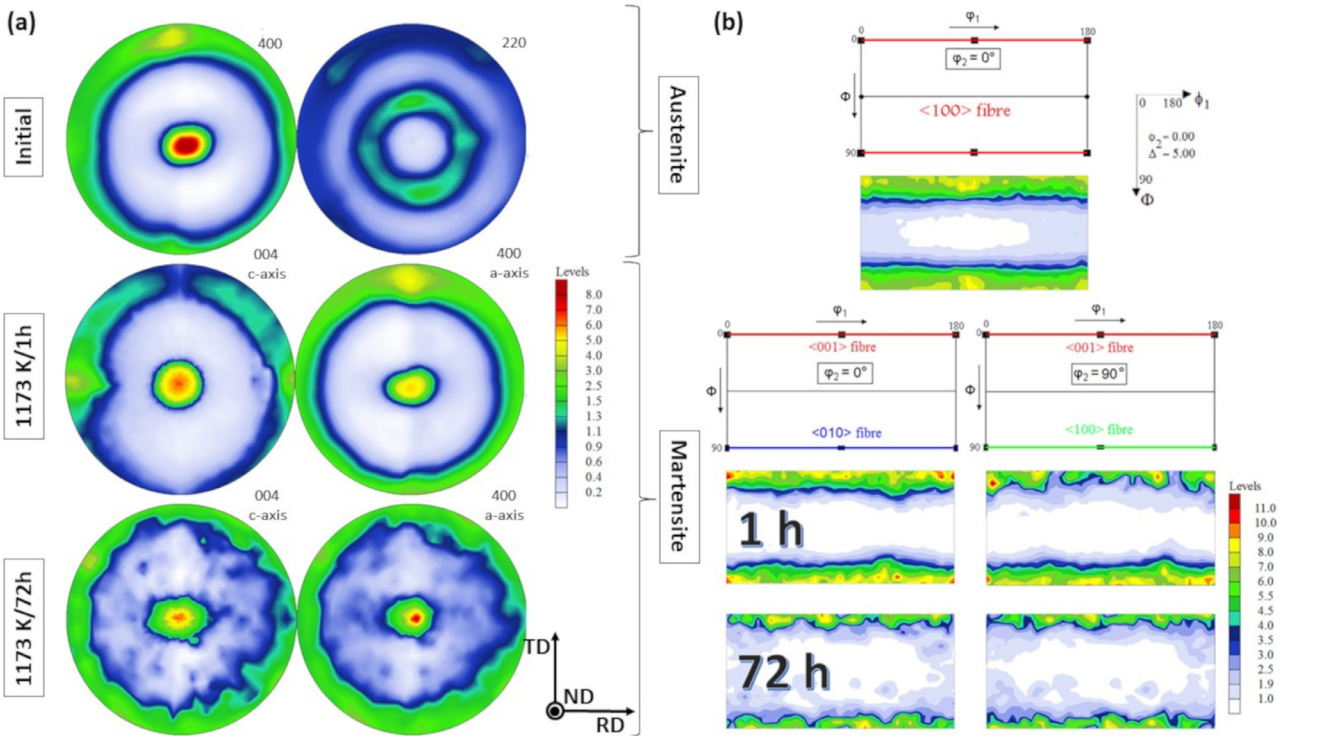

Fig. 9. (a) Complete pole figures recorded by synchrotron X-Ray diffraction, and (b) ODF for initial as-spun and heat treated at 1173 K/1 h and 1173 K/ 72 h Ni-Mn-Ga ribbons.

to a large MFIS value along ND. Moreover, no lateral cracking of cross-section areas is observed.

To expose the global texture of the as-spun and heat-treated at 1173 K/1 h and 1173 K/ 72 h, the complete pole figures were recorded by X-ray synchrotron measurements, Fig. 9 (a). As-spun ribbon (austenitic ones), consistently with EBSD results, has a <100> fiber texture and a cube component, which corresponds to the orientation revealed with EBSD measurement in region 2. The calculated volume fraction of <100> fiber with a spread of ± 12.5° amounts to 79%. Annealing does not change qualitatively the texture (the volume fraction of <100> component remains at the level of 80%), however, it changes the distribution along the <100> axis making it more homogenous. On annealing, the grain structure coarsened, while the near equiaxed grains grow to consume the elongated slab-like shape grains. This process is strongly associated with the texture evolution which also becomes more homogenous eliminating the cube component presented in Figs. 7 and 9. This evolution can be even more pronounced if using ODF sections. Fig. 9(b) shows the ODF sections for the constant $\phi_2 = 0°$ of as-spun and $\phi_2 = 0°$ as well as $\phi_2 = 90°$ heat-treated at 1173 K/1 h and 1173 K/72 h ribbons. It can be noticed that the initial as-spun ribbon and that annealed at 1173 K/1 h exhibit a {001}<100> component (C), while for the sample treated at 1173 K for 72 h the strong cube component disappears which results in a more uniform orientation distribution of the <001> fiber in the ribbon plane. Additionally, the original <100> austenitic fiber texture is divided into three fibers (<100>, <010>, <001>) marked with different colors in the ODF key figures as a result of martensitic transformation, Fig. 9b.

3.3. Magnetic-field induced strain

Fig. 10 presents magnetization loops for ribbons annealed at 1173 K/1 h (a) and 1173 K/72 h (b) recorded at 300 K in a magnetic field directed perpendicular to the plane of the ribbon. The small insets show the first (1') and second (2') magnetization curves. In both cases, with increasing the magnetic field, the increase in magnetization occurs, while small jumps are noticeable (marked by black arrows). Three jumps are apparent for ribbon annealed at 1173 K/1 h while the first step is detected in a magnetic field of 3330 Oe. Ribbon heat-treated at 1173 K/ 72 h shows four jumps with the first one occurring in lower field of 980 Oe. The observed jumps of M(H) may be connected with magnetically induced reorientation of twin variants (MIR) in the martensite state. The low temperature martensite phase is composed of differently oriented twin variants separated by highly mobile twin boundaries. When a magnetic field is applied, the privileged variant grows at the expense of the other differentially oriented variants (exchanging the *a*- and *c*-axes), while jumps correspond to the change from hard (*a*-axis) to easy (*c*-axis) magnetization axis. Interestingly, the jumps have twofold character - vertical and horizontal. The horizontal lines may indicate hindering of twin boundary motion but the vertical ones some reorientation. However, the effect observed in ribbons is not as spectacular as in the case of single crystalline materials due to polycrystalline nature of specimens and very small thickness (demagnetization effect). In single crystals the switching of martensite variants occurs in the entire volume of material, which is observed in large jump in M(H) curves while in the case of polycrystalline ribbons, the martensite variant motion is constrained by grain boundaries. Furthermore, as it can be noticed, the "jumps" become sharper (more martensite variants were shifted) when the extending of annealing time and increase of mean grain size giving rise to higher MFIS value. The effect observed during M(H) measurements (*in-situ*), in which magnetic field was applied and switched in the range of 20000—20000 Oe seems to be partially "magneto-elastic MFIS" being evidenced by steps and humps in each curve, whereas when a magnetic field is once applied and removed the effect is per-

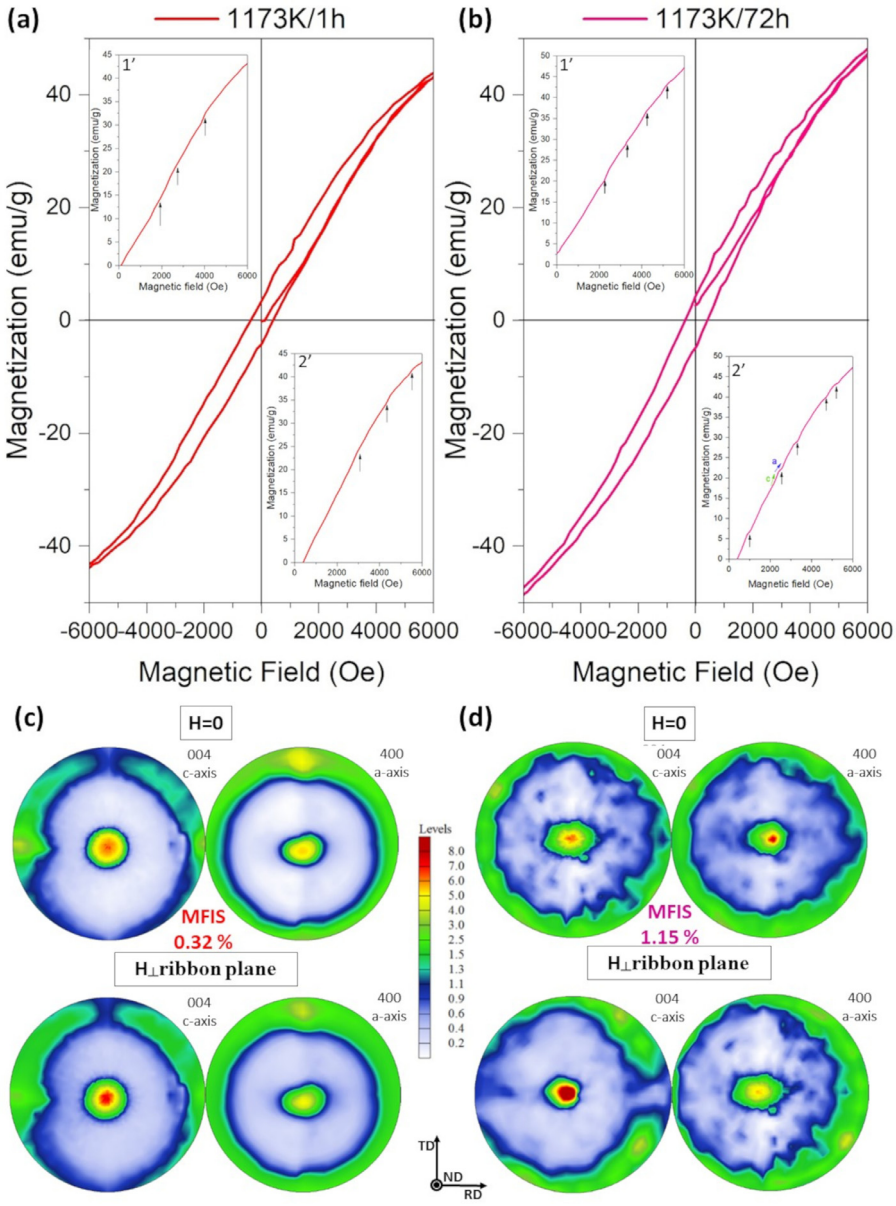

Fig. 10. (a), (b) Magnetization loops for ribbons annealed at 1173 K for 1 h and 72 h measured at 573 K in magnetic field direction perpendicular to the ribbon plane. Smaller insets show the first (1') and second (2') magnetization curves;(c), (d) Complete pole figures for ribbons annealed at 1173 K/1 h(a) and 1173 K/72 h at zero magnetic field ($H = 0$), as well as with magnetic field applied perpendicular to ribbon plane ($H_{\perp}0$), respectively, recorded by synchrotron X-Ray diffraction method.

manent, which was evidenced by both texture analysis and SEM observations. However, to estimate the elastic contribution which the narrow hysteresis is pointing to, *in-situ* texture measurements with switching on and off the magnetic field have to be carried out.

In order to evaluate the magnitude of MFIS, texture measurements were performed. Direct strain measurements were not conducted due to the very small thickness of the sample. For such cases, texture measurements are much more precise. The error for calculating the volume fraction of <004> and <400> texture components by intensity analysis, was estimated to be 1% which then translates to about 0.06% of MFIS. It is worth mentioning that three texture measurements taken on the initial sample at different regions were practically identical. Thus within the given volume fraction (1 mm × 1 mm (beam size) × 10 ribbons), the samples are very homogenous. However, to ensure a direct comparison the texture measurements for MFIS calculations originate exactly from the same positions of the samples. MFIS values were estimated from the volume fraction calculations using the following equation:

$$e_{MFIS} = \left(1 - \frac{c}{a}\right) \cdot V_{fiber} \cdot V_C,$$

where a and c are lattice parameters of martensite and this term corresponds to the maximum theoretical MFIS in <100> oriented single crystals, then V_{fiber} is a volume fraction of <100> fiber, V_c is a volume fraction of variants in which the c-axis was reoriented along the ND after the application of a magnetic field. Taking into account the lattice parameters ($a = 5.952$ Å, $c = 5.584$ Å) and the volume fraction of the fiber texture (80%) the obtained results are consistent with magnetic measurements where only about 6.5% of fiber volume fraction reorients its c-axis towards ND in the 1173 K/1 h sample resulting in about 0.32% of texture determined MFIS, whereas circa 24% volume reorientation takes place in the 1173 K/72 h ribbons producing about 1.15% texture evaluated MFIS.

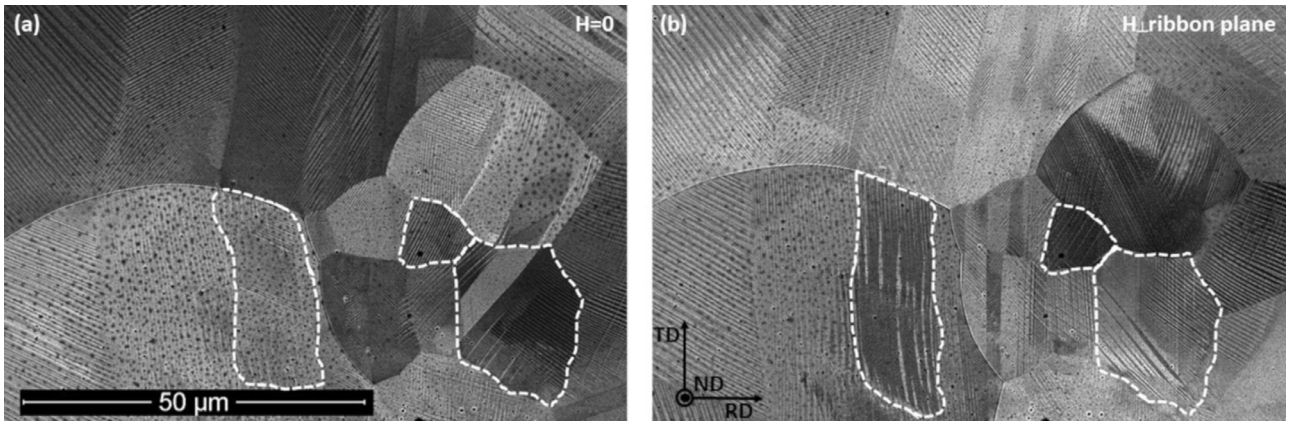

Fig. 11. SEM/BSE images taken from the free side of ribbon annealed at 1173 K/72 h in the initial state (a), and after magnetic field applied perpendicular to ribbon plane (b).

It has to be pointed out that the given MFIS values are permanent as during measurement no magnetic field was applied (magnetic field was removed). The direction of the obtained strain is negative along ND since more *c*-axis is aligned along this direction. On the other hand, sample elongation is obtained perpendicular to the magnetic field and lays radially in the ribbon plane.

It is hence demonstrated that reorientation of variants is possible using only magnetic field without any assistance of mechanical force on self-accommodated Ni-Mn-Ga material. The variant reorientation can be directly seen in Fig. 11, where practically every grain undergoes twin rearrangement under an application of the magnetic field. The most spectacular ones are highlighted with dashed white lines. This implies that every single grain contributes to MFIS ensuring a homogenous in-plane deformation. In this context, the strong fiber texture and relatively homogenous microstructure establish the conditions for isotropic in-plane plastic response. This in turn enables easy twin boundary motion and no crack formation.

It should be mentioned that the reason for selecting only magnetic field to reorient martensitic variants (no mechanical stress) is twofold. On the one hand, it shows that MFIS is prone to appear in self-accommodated state which is relevant in terms of overheating and back transformation to austenite. In such a case the material can restore its functional properties by using only magnetic field (no mechanical training procedure is required). On the other hand, by using magnetic field only a limited stress of about 3 MPa, resulting from magneto-crystalline anisotropy energy can be achieved. This effectively prevents material degradation and crack formation. It should be also noted that the obtained MFIS values can be significantly larger, when exposed to a series of magnetic training. Nevertheless, for back reorientation (*c*-axis in ribbon plane) a rotating magnetic field has to be applied. However, due to the complexity of this process, the reverse twin boundary motion and the exact strain accommodation mechanism will be subjects of another study.

4. Conclusions

In this work, we have examined the microstructure and crystallographic texture of $Ni_{50.2}Mn_{28.3}Ga_{21.5}$ melt-spun ribbons subjected to heat treatment under various conditions. It was demonstrated that with the increase of annealing temperature both martensitic and magnetic transformations were shifted to higher temperatures being related to an increase in atomic order degree rather than the grain size growth. As annealing temperature rises, the volume fraction of 10M martensite increases achieving complete transformation. Moreover, heat treatment ensures homogenous radial microstructure of the ribbons having a strong <100> fiber texture giving rise to MFIS. We have shown that self-accommodated 10M $Ni_{50.2}Mn_{28.3}Ga_{21.5}$ melt-spun ribbons subjected to heat treatment at 1173 K/72 h exhibit MFIS as high as 1.15% without mechanical training. The MFIS magnitude is comparatively large for polycrystalline material. The obtained grain size with the value amounting to the ribbon thickness reduces incompatibility between neighboring grains being beneficial for strain accommodation during variant reorientation.

Declaration of Competing Interest

The authors declare that they have no known competing financial interests or personal relationships that could have appeared to influence the work reported in this paper.

Acknowledgement

National Centre for Research and Development (NCBiR) of Poland is acknowledged for funding (TECHMATSTRATEG 2/410941/4/NCBR/2019).

References

[1] K. Ullakko, J.K. Huang, C. Kantner, R.C.O' Handley, V.V. Kokorin, Large magnetic field-induced strains in Ni_2MnGa single crystals, Appl. Phys. Lett. 69 (1996) (1966), doi:10.1063/1.117637.
[2] E. Pagounis, R. Chulist, M.J. Szczerba, M. Laufenberg, Over 7% magnetic field-induced strain in a Ni-Mn-Ga five-layered martensite, Appl. Phys. Lett. 105 (2014) 052405, doi:10.1063/1.4892633.
[3] E. Pagounis, M.J. Szczerba, R. Chulist, M. Laufenberg, Large magnetic field-induced work output in a NiMnGa seven-layered modulated martensite, Appl. Phys. Lett. 107 (2015) 152407, doi:10.1063/1.4933303.
[4] A. Sozinov, N. Lanska, A. Soroka, W. Zou, 12% magnetic field-induced strain in Ni-Mn-Ga-based non-modulated martensite, Appl. Phys. Lett. 102 (2013) 021902, doi:10.1063/1.4775677.
[5] I. Suorsa, J. Tellinen, K. Ullakko, E. Pagounis, Voltage generation induced by mechanical straining in magnetic shape memory materials, J. Appl. Phys. 95 (2004) 8054, doi:10.1063/1.1711181.
[6] N. Sarawate, M. Dapino, Experimental characterization of the sensor effect in ferromagnetic shape memory Ni-Mn-Ga, Appl. Phys. Lett. 88 (2006) 121923, doi:10.1063/1.2189452.
[7] I. Karaman, B. Basaran, H.E. Karaca, A.I. Karsilayan, Y.I. Chumlyakov, Energy harvesting using martensite variant reorientation mechanism in a NiMnGa magnetic shape memory alloy, Appl. Phys. Lett. 90 (2007) 172505, doi:10.1063/1.2721143.
[8] H.E. Karaca, I. Karaman, B. Basaran, Y. Ren, Y.I. Chumlyakov, H.J. Maier, Magnetic field-induced phase transformation in NiMnCoIn magnetic shape memory alloys - a new actuation mechanism with large work output, Adv. Funct. Mater. 19 (2009) 983, doi:10.1002/adfm.200801322.
[9] S. Barker, E. Rhoads, P. Lindquist, M. Vreugdenhil, P. Mullner, Magnetic shape memory micropump for submicroliter intracranial drug delivery in rats, J. Med. Device 10 (2016) 041009, doi:10.1115/1.4034576.

[10] N.M. Bruno, C. Ciocanel, H.P. Feigenbaum, A. Waldauer, A theoretical and experimental investigation of power harvesting using the NiMnGa martensite reorientation mechanism, Smart Mater. Struct. 21 (2012) 094018, doi:10.1088/0964-1726/21/9/094018.

[11] D.C. Dunand, P. Müllner, Size effects on magnetic actuation in Ni-Mn-Ga shape-memory alloys, Adv. Mater. 23 (2011) 216, doi:10.1002/adma.201002753.

[12] U. Gaitzsch, S. Roth, B. Rellinghaus, L. Schultz, Adjusting the crystal structure of NiMnGa shape memory ferromagnets, J. Magn. Magn. Mater. 305 (2006) 275, doi:10.1016/j.jmmm.2006.01.017.

[13] U. Gaitzsch, J. Romberg, M. Potschke, S. Roth, P. Müllner, Stable magnetic-field-induced strain above 1% in polycrystalline Ni–Mn–Ga, Scr. Mater. 65 (2011) 679, doi:10.1016/j.scriptamat.2011.07.011.

[14] M. Pötschke, U. Gaitzsch, S. Roth, B. Rellinghaus, L. Schultz, Preparation of melt textured Ni–Mn–Ga, J. Magn. Magn. Mater. 316 (2007) 383, doi:10.1016/j.jmmm.2007.03.032.

[15] K. Ullakko, Y. Ezer, A. Sozinov, G. Kimmel, P. Yakovenko, V. Lindroos, Magnetic-field-induced strains in polycrystalline Ni-Mn-Ga at room temperature, Scr. Mater. 44 (2001) 475, doi:10.1016/S1359-6462(00)00610-2.

[16] U. Gaitzsch, M. Potschke, S. Roth, B. Rellinghaus, L. Schultz, A 1% magnetostrain in polycrystalline 5M Ni–Mn–Ga, Acta Mater. 57 (2009) 365, doi:10.1016/j.actamat.2008.09.017.

[17] C. Hürrich, S. Roth, H. Wendrock, M. Potschke, D. Cong, B. Rellinghaus, L. Schultz, Influence of grain size and training temperature on strain of polycrystalline $Ni_{50}Mn_{29}Ga_{21}$ samples, J. Phys. Conf. Ser. 303 (2011) 012080, doi:10.1088/1742-6596/303/1/012080.

[18] N. Scheerbaum, O. Heczko, J. Liu, D. Hinz, L. Schultz, O. Gutfleisch, Magnetic field-induced twin boundary motion in polycrystalline Ni-Mn-Ga fibers, New J. Phys. 10 (2008) 073002, doi:10.1088/1367-2630/10/7/073002.

[19] V. Zhukova, V. Rodionova, L. Fetisov, A. Grunin, A. Goikhman, A. Torcunov, A. Aronin, G. Abrosimova, A. Kiselev, N. Perov, A. Granovsky, T. Ryba, S. Michalik, Magnetic properties of Heusler-type microwires and thin films, IEEE Trans. Magn. 50 (2014) 4, doi:10.1109/TMAG.2014.2324494.

[20] V. Rodionova, M. Ilyn, A. Granovsky, N. Perov, V. Zhukova, G. Abrosimova, A. Aronin, A. Kiselev, A. Zhukov, Internal stress induced texture in Ni-Mn-Ga based glass-covered microwires, J. Appl. Phys. 114 (2013) 123914, doi:10.1063/1.4822168.

[21] M. Chmielus, X.X. Zhang, C. Witherspoon, D.C. Dunand, P. Müllner, Giant magnetic-field-induced strains in polycrystalline Ni–Mn–Ga foams, Nat. Mater. 8 (2009) 863, doi:10.1038/nmat2527.

[22] Y. Boonyongmaneerat, M. Chmielus, D.C. Dunand, P. Müllner, Increasing magnetoplasticity in polycrystalline Ni-Mn-Ga by reducing internal constraints through porosity, Phys. Rev. Lett. 99 (2007) 1, doi:10.1103/PhysRevLett.99.247201.

[23] C. Witherspoon, P. Zheng, M. Chmielus, D.C. Dunand, P. Müllner, Effect of porosity on the magneto-mechanical behavior of polycrystalline magnetic shape-memory Ni-Mn-Ga foams, Acta Mater. 92 (2015) 64, doi:10.1016/j.actamat.2015.03.038.

[24] P. Zheng, N.J. Kucza, Z. Wang, P. Mullner, D.C. Dunand, Effect of directional solidification on texture and magnetic-field-induced strain in Ni-Mn-Ga foams with coarse grains, Acta Mater. 86 (2015) 95, doi:10.1016/j.actamat.2014.12.005.

[25] M. Chmielus, C. Witherspoon, R.C. Wimpory, A. Paulke, A. Hilger, X. Zhang, D.C. Dunand, P. Mullner, Magnetic-field-induced recovery strain in polycrystalline Ni-Mn-Ga foam, J. Appl. Phys. 108 (2010) 123526, doi:10.1063/1.3524503.

[26] F. Nilsen, J. Lehtonen, Y. Ge, I. Aaltio, S.P. Hannula, Highly porous spark plasma sintered Ni-Mn-Ga structures, Scr. Mater. 139 (2017) 148, doi:10.1016/j.scriptamat.2017.06.040.

[27] J. Wang, Y. Han, H. Hua, X. Wang, Ch. Jiang, Grain size effect on the martensitic transformation of $Ni_{50}Mn_{25}Ga_{17}Cu_8$ high-temperature shape memory alloy, Intermetallics 61 (2015) 42, doi:10.1016/j.intermet.2015.02.016.

[28] S.Y. Yu, A.J. Gu, S.S. Kang, S.J. Hu, Z.C. Li, S.T. Ye, H.H. Li, J.J. Sun, R.R. Hao, Large reversible magnetostrain in polycrystalline $Ni_{50}Mn_{33}In_{17-x}Ga_x$, J. Alloys Compd. 681 (2016) 1, doi:10.1016/j.jallcom.2016.04.249.

[29] L. Zhou, A. Giri, K. Cho, Y. Sohn, Mechanical anomaly observed in Ni-Mn-Ga alloys by nanoindentation, Acta Mater. 118 (2016) 54, doi:10.1016/j.actamat.2016.07.029.

[30] F. Chen, B. Tian, L. Li, Y. Zheng, Phase transformation and microstructure of Ni–Mn–Ga ferromagnetic shape memory alloy particles, Phys. Scr. T129 (2007) 227, doi:10.1088/0031-8949/2007/T129/051.

[31] D.M. Liu, Z.H. Nie, Y.D. Wang, Y.D. Liu, G. Wang, Y. Ren, L. Zuo, New sequences of phase transition in Ni-Mn-Ga ferromagnetic shape memory nanoparticles, Metall. Mater. Trans. A 39 (2008) 466, doi:10.1007/s11661-007-9435-8.

[32] B. Tian, F. Chen, Y. Liu, Y.F. Zheng, Structural transition and atomic ordering of $Ni_{49.8}Mn_{28.5}Ga_{21.7}$ ferromagnetic shape memory alloy powders prepared by ball milling, Mater. Lett. 62 (2008) 2851, doi:10.1016/j.matlet.2008.01.071.

[33] P. Czaja, R. Chulist, A. Wójcik, M. Kowalczyk, P. Zackiewicz, A. Szewczyk, N. Schell, W. Maziarz, Supression and recovery of martensitic transformation and magnetism in mechanically and thermally treated magnetic shape memory Ni-Mn-Ga melt-spun ribbons, Adv. Eng. Mater. (2021), doi:10.1002/adem.202100075.

[34] T.D. Hatchard, J.S. Thorne, S.P. Farrell, R.A. Dunlap, Production of $Ni_{100-x-y}Mn_xGa_y$ magnetic shape memory alloys by mechanical alloying, J. Phys. Condens. Matter 20 (2008) 445205, doi:10.1088/0953-8984/20/44/445205.

[35] V.A. Chernenko, E. Cesari, J. Pons, C. Segui, Phase Transformations in rapidly quenched Ni-Mn-Ga alloys, J. Mater. Res. 15 (2000) 1496, doi:10.1557/JMR.2000.0215.

[36] O. Heczko, P. Svec, D. Janickovic, K. Ullakko, Magnetic properties of Ni-Mn-Ga ribbon prepared by rapid solidification, IEEE Trans. Magn. 38 (2002) 2841, doi:10.1109/TMAG.2002.802471.

[37] N.V. Rama Rao, R. Gopalan, V. Chandrasekaran, K.G. Suresh, Microstructure, magnetic properties and magnetocaloric effect in melt-spun Ni–Mn–Ga ribbons, J. Alloys Compd. 478 (2009) 59, doi:10.1016/j.jallcom.2008.12.015.

[38] J. Gutiérrez, J.M. Barandiarán, P. Lázpita, C. Seguí, E. Cesari, Magnetic properties of a rapidly quenched Ni–Mn–Ga shape memory alloy, Sens. Actuators A Phys. 129 (2020) 163, doi:10.1016/j.sna.2005.11.035.

[39] P. Lázpita, G. Rojo, J. Gutiérrez, J.M. Barandiaran, R.C. O'Handley, Correlation between magnetization and deformation in a NiMnGa shape memory alloy Polycrystalline ribbon, Sens. Lett. 5 (2007) 65, doi:10.1166/sl.2007.033.

[40] A.K. Panda, M. Ghosh, A. Kumar, A. Mitra, Magnetic transitions and structure of a NiMnGa ferromagnetic shape memory alloy prepared by melt spinning technique, J. Magn. Magn. Mater. 320 (2008) L116, doi:10.1016/j.jmmm.2008.03.055.

[41] N. Scheerbaum, O. Heczko, J. Liu, D. Hinz, L. Schultz, O. Gutfleisch, Magnetic field-induced twin boundary motion in polycrystalline Ni–Mn–Ga fibers, N. J. Phys. 10 (2008) 073002, doi:10.1088/1367-2630/10/7/073002.

[42] Z. Li, Y. Jiang, Z. Li, Y. Yang, B. Yang, Y. Zhang, C. Esling, X. Zhao, L. Zuo, Texture inheritance from austenite to 7 M martensite in Ni–Mn–Ga melt-spun ribbons, Results Phys. 6 (2016) 428, doi:10.1016/j.rinp.2016.07.012.

[43] F. Albertini, S. Besseghini, A. Paoluzi, L. Pareti, M. Pasquale, F. Passaretti, C.P. Sasso, A. Stantero, E. Villa, Structural, magnetic and anisotropic properties of Ni_2MnGa melt-spun ribbons, J. Magn. Magn. Mater. 242–245 (2002) 1421, doi:10.1016/S0304-8853(01)00992-1.

[44] Z.H. Liu, J.L. Chen, H.N. Hu, M. Zhang, X.F. Dai, Z.Y. Zhu, G.D. Liu, G.H. Wu, F.B. Meng, Y.X. Li, The influence of heat treatment on the magnetic and phase transformation properties of quaternary Heusler alloy $Ni_{50}Mn_8Fe_{17}Ga_{25}$ ribbons, Scr. Mater. 51 (2004) 1011, doi:10.1016/j.scriptamat.2004.07.005.

[45] B.Z. Li, J. Wang, Y. Zhang, K. He, X. Zhao, L. Zuo, G. Hofer, C. Esling, Texturation of Ni–Co–Mn–In ribbons by melt spinning, Adv. Eng. Mater. 12 (2010) 1024, doi:10.1002/adem.201000073.

[46] C. Randau, U. Garbe, H.G. Brokmeier, Stress texture calculator: a software tool to extract texture, strain and microstructure information from area-detector measurements, J. Appl. Crystallogr. 44 (2011) 641, doi:10.1107/S0021889811012064.

[47] V. Sanchez-Alarcos, J.I. Perez-Landazabal, V. Recarte, G.J. Cuello, Correlation between atomic order and the characteristics of the structural and magnetic transformations in Ni-Mn-Ga shape memory alloys, Acta Mater. 55 (2007) 3883, doi:10.1016/j.actamat.2007.03.001.

[48] V. Sanchez-Alarcos, J.I. Perez-Landazabal, V. Recarte, J.A. Rodriguez-Velamazan, V.A. Chernenko, Effect of atomic order on the martensitic and magnetic transformations in Ni–Mn–Ga ferromagnetic shape memory alloys, J. Phys. Condens. Metter. 22 (2010) 166001, doi:10.1088/0953-8984/22/16/166001.

[49] R. Chulist, P. Czaja, On the role of atomic shuffling in the 4O, 4M and 8M martensite structures in Ni-Mn-Sn single crystal, Scr. Mater. 189 (2020) 106, doi:10.1016/j.scriptamat.2020.08.007.

[50] R. Chulist, M. Faryna, M.J. Szczerba, Orientation relationship between austenite and non-modulated martensite in Ni–Mn–Ga single crystals, Acta Mater. 103 (2016) 836, doi:10.1016/j.actamat.2015.11.007.

[51] R. Chulist, K. Nalepka, A. Sozinov, Hierarchical twin microstructure in modulated 10M Ni–Mn-Ga single crystals. An analysis including shuffling of atomic layers, Int. J. Plast. 126 (2020) 102628, doi:10.1016/j.ijplas.2019.11.007.

[52] P.J. Webster, Heusler alloys, Contemp. Phys. 10 (6) (1969) 559, doi:10.1080/00107516908204800.

[53] P.J. Webster, K.R.A. Ziebeck, S.L. Town, M.S. Peak, Magnetic order and phase transformation in Ni_2MnGa, Philos. Mag. B 49 (3) (1984) 295, doi:10.1080/13642817408246515.

[54] M.E. Gruner, R. Niemann, P. Entel, R. Pentcheva, U.K. Rößler, K Nielsch, S Fähler, Modulations in martensitic Heusler alloys originate from nanotwin ordering, Sci. Rep. 8 (2018) 8489, doi:10.1038/s41598-018-26652-6.

[55] V.A. Chernenko, Compositional instability of β-phase in Ni-Mn-Ga alloys, Scr. Mater. 40 (1999) 523, doi:10.1016/S1359-6462(98)00494-1.

[56] X. Jin, M. Marioni, D. Bono, S.M. Allen, R.C. O'Handley, T.Y. Hsu, Empirical mapping of Ni–Mn–Ga properties with composition and valence electron concentration, J. Appl. Phys. 91 (2002) 8222, doi:10.1063/1.1453943.

[57] J. Wang, C. Jiang, R. Techapiesancharoenkij, D. Bono, S.M. Allen, R.C. O'Handley, Microstructure and magnetic properties of melt spinning Ni-Mn-Ga, Intermetallics 32 (2013) 151, doi:10.1016/j.intermet.2012.08.021.

[58] M. Kreissl, K.U. Neumann, T. Stephens, K.R.A. Ziebeck, The influence of atomic order on the magnetic and structural properties of the ferromagnetic shape memory compound Ni_2MnGa, J. Phys. Condens. Matter 15 (2003) 3831, doi:10.1088/0953-8984/15/22/317.

[59] B. Cantor, W.T. Kim, B.P. Bewlay, A.G. Gillen, Microstructure-cooling rate correlations in melt-spun alloys, J. Mater. Sci. 26 (1991) 1266, doi:10.1007/bf00544465.